Applications of plane-wave destructor filters

Sergey Fomel[1]

ABSTRACT

On several synthetic and real-data examples, I show that finite-difference plane-wave destructor filters can be a valuable alternative to prediction-error filters in applications such as data interpolation, fault detection, and noise attenuation.

INTRODUCTION

Plane-wave destructor filters, introduced in *Processing Versus Inversion* (Claerbout, 1992a), serve the purpose of characterizing seismic images by a superposition of local plane waves. They are constructed as finite-difference stencils for the plane-wave differential equation. In many cases, a local plane-wave model is a very convenient representation of seismic data. Unfortunately, early experiences with applying plane-wave destructors for interpolating spatially aliased data showed their poor performance in comparison with that of industry-standard F-X prediction-error filters (Spitz, 1991).

For each given frequency, an F-X prediction-error filter (PEF) can be thought of as a Z-transform polynomial. The roots of the polynomial correspond precisely to predicted plane waves (Canales, 1984). Therefore, F-X PEFs simply represent a spectral (frequency-domain) approach to plane-wave destruction. This powerful and efficient approach is, however, not theoretically adequate, when the plane wave slopes or the boundary conditions vary both spatially and temporally.

Multidimensional T-X prediction-error filters (Claerbout, 1992a, 1999) share the same purpose of predicting local plane waves. They work well with spatially aliased data and allow for both temporal and spatial variability of the slopes. In practice, however, T-X filters appear as very mysterious creatures, because their construction involves many non-intuitive parameters. The user needs to choose such parameters as the number of filter coefficients, the gap and the exact shape of the filter, the size, number, and shape of local patches for filter estimation, the number of iterations and the amount of regularization. Recently developed techniques for handling non-stationary PEFs (Crawley et al., 1998, 1999; Clapp et al., 1999; Crawley, 1999), demonstrated an excellent performance in a variety of applications (Brown et al., 1999; Clapp and Brown, 2000; Crawley, 2000), but the large number of adjustable parameters still requires a significant human interaction and remains the down side of the method.

Clapp et al. (1997) have recently revived the original plane-wave destructors for precondi-

---

[1]**email:** sergey@sep.stanford.edu

tioning tomographic problems with predefined dip field (Clapp et al., 1998; Clapp and Biondi, 1998, 2000). The filters were named *steering filters* because of their ability to steer the solution in the direction of the local dips.

In this paper, I revisit Claerbout's original technique of finite-difference plane-wave destruction. First, I develop an approach for increasing the accuracy and dip bandwidth of the method. Applying the improved filter design to several data interpolation and noise attenuation problems, I discover that the finite-difference filters often perform as well as or even better than T-X PEFs. At the same time, the number of adjustable parameters is kept at minimum, and the only estimated quantity has a clear physical meaning of the local plane-wave slope.

The encouraging results of this paper suggest further experiments with plane-wave destructors. One can apply similar approaches to wave fields, characterized by more complicated differential equations, such as the offset continuation equation (Fomel, 2000c).

HIGH-ORDER PLANE-WAVE DESTRUCTORS

The mathematical basis of the plane-wave destructor filters is the local plane differential equation

$$\frac{\partial P}{\partial x} + s\,\frac{\partial P}{\partial t} = 0 \,, \tag{1}$$

where $P(t,x)$ is the wave field, and s is the local slope, which may also depend on t and x. In the case of a constant slope, equation (1) has the simple general solution

$$P(t,x) = f(t - sx) \,, \tag{2}$$

where $f(t)$ is an arbitrary waveform. Equation (2) is nothing more than a mathematical description of a plane wave.

If the slope s does not depend on the t coordinate, we can transform equation (1) to the frequency domain, where it takes the form of the ordinary differential equation

$$\frac{d\hat{P}}{dx} + i\omega s\,\hat{P} = 0 \tag{3}$$

and has the general solution

$$\hat{P}(x) = \hat{P}(0)\,e^{i\omega sx} \,, \tag{4}$$

where $\hat{P}$ is the Fourier transform of P. The complex exponential term in equation (4) simply represents a shift of a t-trace according to the slope s and the trace separation x. In the frequency domain, the operator for transforming the trace at position $x - 1$ to the neighboring trace at position x is a multiplication by $e^{i\omega s}$. In other words, a plane wave can be perfectly predicted by a two-term prediction-error filter in the F-X domain:

$$a_0\,\hat{P}(x) + a_1\,\hat{P}(x - 1) = 0 \,, \tag{5}$$

where $a_0 = 1$ and $a_1 = -e^{-i\omega s}$. The goal of predicting several plane waves can be accomplished by cascading several two-term filters. In fact, any $F\text{-}X$ prediction-error filter, represented in the Z-transform form as

$$A(Z_x) = 1 + a_1 Z_x + a_2 Z_x^2 + \cdots + a_N Z_x^N \, , \tag{6}$$

can be factored into a product of two-term filters:

$$A(Z_x) = \left(1 - \frac{Z_x}{Z_1}\right)\left(1 - \frac{Z_x}{Z_2}\right) \cdots \left(1 - \frac{Z_x}{Z_N}\right) \, , \tag{7}$$

where $Z_1, Z_2, \ldots, Z_N$ are the zeroes of polynomial (6). According to equation (5), the phase of each zero corresponds to the slope of a local plane wave multiplied by the frequency. Zeroes that are not on the unit circle carry an additional amplitude gain not included in equation (3).

In order to incorporate time-varying slopes, we need to return back to the time domain and look for an appropriate analog of the phase-shift operator (4) and the plane-prediction filter (5). An important property of plane-wave propagation across different traces is that the total energy of the transmitted wave stays invariant throughout the process. This property is assured in the frequency-domain solution (4) by the fact that the spectrum of the complex exponential $e^{i\omega s}$ is equal to one. In the time domain, we can reach an equivalent effect by using an all-pass digital filter. In the Z-transform notation, convolution with an all-pass filter takes the form

$$\hat{P}_{x+1}(Z_t) = \hat{P}_x(Z_t) \frac{B(Z_t)}{B(1/Z_t)} \, , \tag{8}$$

where $\hat{P}_x(Z_t)$ denotes the Z-transform of the corresponding trace, and the ratio $B(Z_t)/B(1/Z_t)$ is an all-pass digital filter, approximating the time-shift operator (5). In finite-difference terms, equation (8) represents an implicit finite-difference scheme for solving equation (1) with the initial conditions at a constant x. The coefficients of filter $B(Z_t)$ can be determined, for example, by fitting the filter frequency response at small frequencies to the response of the phase-shift operator. The Taylor series technique (equating the coefficients of the Taylor series expansion around zero frequency) yields the expression

$$B_3(Z_t) = \frac{(1-s)(2-s)}{12} Z_t^{-1} + \frac{(2+s)(2-s)}{6} + \frac{(1+s)(2+s)}{12} Z_t \tag{9}$$

for a three-point centered filter $B_3(Z_t)$ and the expression

$$
\begin{aligned}
B_5(Z_t) \;=\; & \frac{(1-s)(2-s)(3-s)(4-s)}{1680} Z_t^{-2} + \frac{(4-s)(2-s)(3-s)(4+s)}{420} Z_t^{-1} + \\
& \frac{(4-s)(3-s)(3+s)(4+s)}{280} + \\
& \frac{(4-s)(2+s)(3+s)(4+s)}{420} Z_t + \frac{(1+s)(2+s)(3+s)(4+s)}{1680} Z_t^2
\end{aligned}
\tag{10}
$$

for a five-point centered filter $B_5(Z_t)$. It is easy to generalize these expressions to longer filters. Figure 1 shows the phase of the all-pass filters $B_3(Z_t)/B_3(1/Z_t)$ and $B_5(Z_t)/B_5(1/Z_t)$ for two
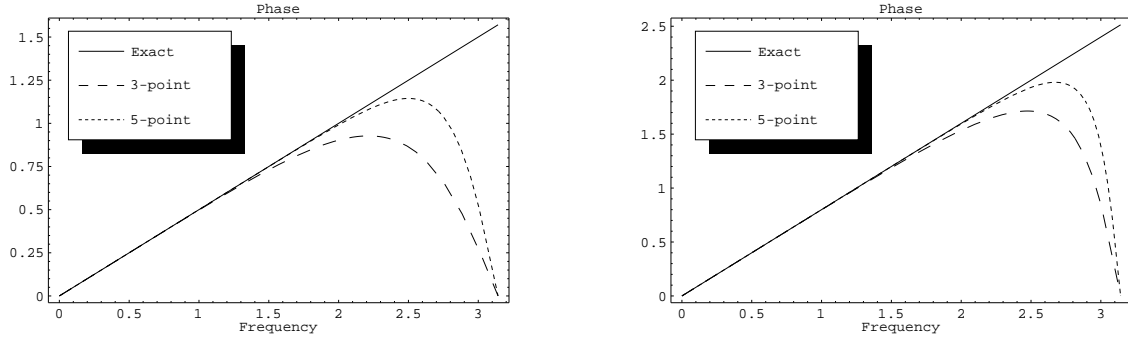
Figure 1: Phase of the implicit finite-difference shift operators in comparison with the exact solution. Left plot corresponds to $s = 0.5$. Right plot; $s = 0.8$. $\boxed{\text{sergey1-phase}}$ [CR]

values of the slope s in comparison with the exact linear function of equation (4). As expected, the phases fit the exact line at low frequencies, and the accuracy of the approximation increases with the length of the filter.

In two dimensions, equation (8) transforms to the prediction equation analogous to (5) with the 2-D prediction filter[2]

$$A(Z_t, Z_x) = 1 - Z_x \frac{B(1/Z_t)}{B(Z_t)} . \tag{11}$$

In order to characterize several plane waves, we can cascade several filters of the form (11) in a manner similar to equation (7). In all examples of this paper, I used a modified version of the filter $A(Z_t, Z_x)$, namely the filter

$$C(Z_t, Z_x) = A(Z_t, Z_x)B(Z_t) = B(Z_t) - Z_x B(1/Z_t) , \tag{12}$$

which avoids the need for polynomial division. In case of the 3-point filter (9), the 2-D filter (12) has exactly six coefficients, with the second t column being a reversed copy of the first column. When filter (12) is used in interpolation problems, it can occasionally cause undesired high-frequency oscillations in the solution, resulting from the near-Nyquist zeroes of the polynomial $B(Z_t)$. The oscillations are easily removed in practice with an appropriate low-pass filtering.

In the next section, I address the problem of estimating the local slope s with the filters of form (12). Estimating the slope is a necessary step for applying the finite-difference plane-wave filters on real data.

---

[2]The helix transform (Claerbout, 1998) would map this 2-D filter to an equivalent 1-D filter by imposing the equality $Z_x = Z_t^{N_t}$, where N_t is the length of the t axis or, equivalently, the diameter of the corresponding helix (Rickett and Guitton, 2000). This transformation is not essential for the further discussion.

SLOPE ESTIMATION

Let us denote by $\mathbf{C}(\mathbf{s})$ the operator of convolving the data with the 2-D filter $C(Z_t, Z_x)$ of equation (12) assuming the local slope $\mathbf{s}$. In order to determine the slope, we can define the least-squares goal

$$\mathbf{C}(\mathbf{s})\,\mathbf{d} \approx 0\,, \tag{13}$$

where $\mathbf{d}$ is the known data, and the approximate equality implies that the solution is found by minimizing the power of the left-hand side. Equations (9) and (10) show that the slope $\mathbf{s}$ enters in the filter coefficients in an essentially non-linear way. However, one can still apply the linear iterative optimization methods by an analytical linearization of equation (13). The linearization implies solving the linear system

$$\mathbf{C}'(\mathbf{s}_0)\,\Delta\mathbf{s}\,\mathbf{d} + \mathbf{C}(\mathbf{s}_0)\,\mathbf{d} \approx 0 \tag{14}$$

for the slope increment $\Delta\mathbf{s}$. Here $\mathbf{s}_0$ is the initial slope estimate, and $\mathbf{C}'(\mathbf{s})$ is a convolution with the filter, obtained by differentiating the filter coefficients of $\mathbf{C}(\mathbf{s})$ with respect to $\mathbf{s}$. After system (13) is solved, the initial slope $\mathbf{s}_0$ is updated by adding $\Delta\mathbf{s}$ to it, and one can solve the linear problem again. Depending on the starting solution, the method may require several non-linear iterations to achieve an acceptable convergence. The described linearization approach is similar in idea to tomographic velocity estimation.

In the case of time- and space-varying slope $\mathbf{s}$, system (14) may lead to undesirably rough slope estimates. Moreover, the solution will be undefined in the regions of unknown or constant data. Both these problems are solved by adding a regularization (styling) goal to system (14). The additional goal takes the form

$$\epsilon\mathbf{D}\,\Delta\mathbf{s} \approx 0\,, \tag{15}$$

where $\mathbf{D}$ is an appropriate roughening operator, and ϵ is a scaling coefficient. For simplicity, I chose $\mathbf{D}$ to be the gradient operator. More efficient and sophisticated helical preconditioning techniques are available (Fomel et al., 1997; Fomel, 2000a).

In theory, estimating two different slopes $\mathbf{s}_1$ and $\mathbf{s}_2$ from the available data is only marginally more complicated. The convolution operator becomes a cascade of $\mathbf{C}(\mathbf{s}_1)$ and $\mathbf{C}(\mathbf{s}_2)$, and the linearization yields

$$\mathbf{C}'(\mathbf{s}_1)\,\mathbf{C}(\mathbf{s}_2)\,\Delta\mathbf{s}_1\,\mathbf{d} + \mathbf{C}(\mathbf{s}_1)\,\mathbf{C}'(\mathbf{s}_2)\,\Delta\mathbf{s}_2\,\mathbf{d} + \mathbf{C}(\mathbf{s}_1)\,\mathbf{C}(\mathbf{s}_2)\,\mathbf{d} \approx 0\,. \tag{16}$$

The regularization condition should now be applied to both $\Delta\mathbf{s}_1$ and $\Delta\mathbf{s}_2$:

$$\epsilon\mathbf{D}\,\Delta\mathbf{s}_1 \;\approx\; 0\,; \tag{17}$$

$$\epsilon\mathbf{D}\,\Delta\mathbf{s}_2 \;\approx\; 0\,. \tag{18}$$

The solution will obviously depend on the initial values of $\mathbf{s}_1$ and $\mathbf{s}_2$, which should not be equal to each other. System (16) is generally under-determined, because it contains twice as

many estimated parameters as equations, but an appropriate choice of the starting solution and the additional regularization conditions allow us to arrive at a practical solution.

The application examples of the next section demonstrate that when the system of equations (14-15) or (16-18) are optimized in the least-squares sense in a cycle of several linearization iterations, it leads to smooth and reliable slope estimates. The regularization conditions (15) and (17-18) assure a smooth extrapolation of the slope to the regions of unknown or constant data.

APPLICATION EXAMPLES

In this section, I examine the performance of the finite-difference plane-destruction filters on several test applications.

Fault detection

The use of prediction-error filters in the problem of detecting local discontinuities was suggested by Claerbout (1992b, 1993, 1999) and further refined by Schwab et al. (1996a,b) and Schwab (1998). Bednar (1997) used simple plane-destructor filters in a similar setting to compute coherency attributes.

To test the performance of the improved plane-wave destructors, I chose several examples from Claerbout (1992b). Figure 2 introduces the first example. The left plot of the figure shows a synthetic model, which resembles sedimentary layers with a plane unconformity and a curvilinear fault. The right plot shows the corresponding "texture" (Brown, 1999; Claerbout and Brown, 1999), obtained by convolving a field of random numbers with the inverse plane-wave destructor filters. The inverse filters were constructed with the B-spline regularization technique (Fomel, 2000b), while the dip field was estimated by the linearization method of the previous section. The dip field itself and the prediction residual [the left-hand side of equation (13)] are shown in the left and right plots of Figure 3 respectively. We observe that the texture plot does reflect the dip structure of the input data, which indicates that the dip field was estimated correctly. The fault and unconformity are clearly visible both in the dip estimate and in the residual plots. Anywhere outside the slope discontinuities and the boundaries, the residual is close to zero. Therefore, it can be used directly as a fault detection measure. Comparing the residual plot in Figure 3 with the analogous plot of Claerbout (1992b) establishes a superior performance of the improved finite-difference destructors in comparison with that of the local $T - X$ prediction-error filters.

Figure 4 shows a simpler synthetic test. The model is composed of linear events with two conflicting slopes. A regularized dip field estimation attempts to smooth the estimated dip in the places where it is not constrained by the data (the left plot of Figure 5.) The corresponding residual (the right plot of Figure 5) shows suppressed linear events and highlights the places of their intersection.

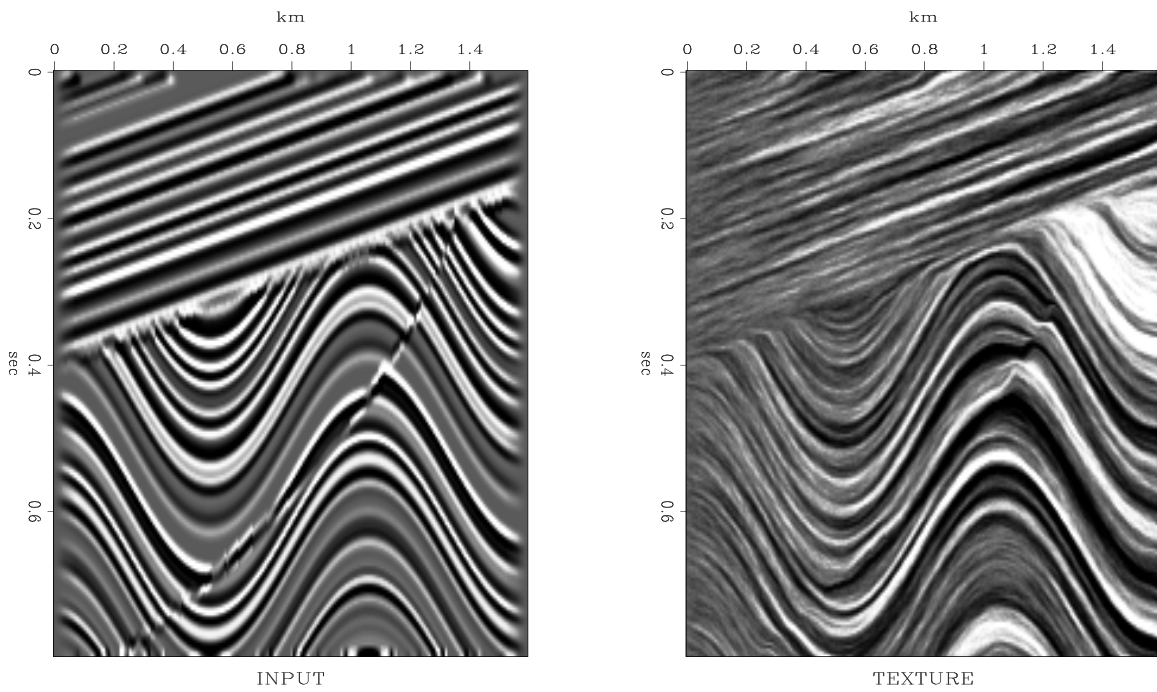The left plot in Figure 6 shows a real shot gather (a portion of Yilmaz and Cumro data

Figure 2: Synthetic sedimentary model. Left plot: Input data. Right plot: Its texture.
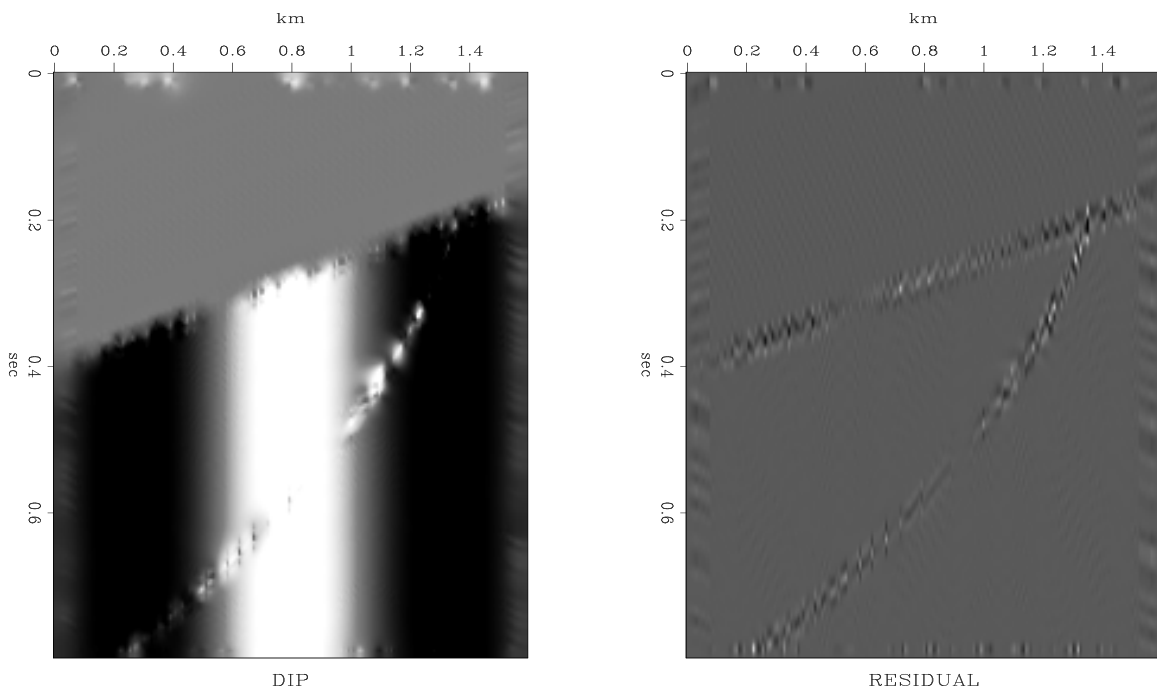sergey1-txtr-sigmoid0 [ER]

Figure 3: Synthetic sedimentary model. Left plot: Estimated dip field. Right plot: Prediction residual. sergey1-lomo2-sigmoid0 [ER]
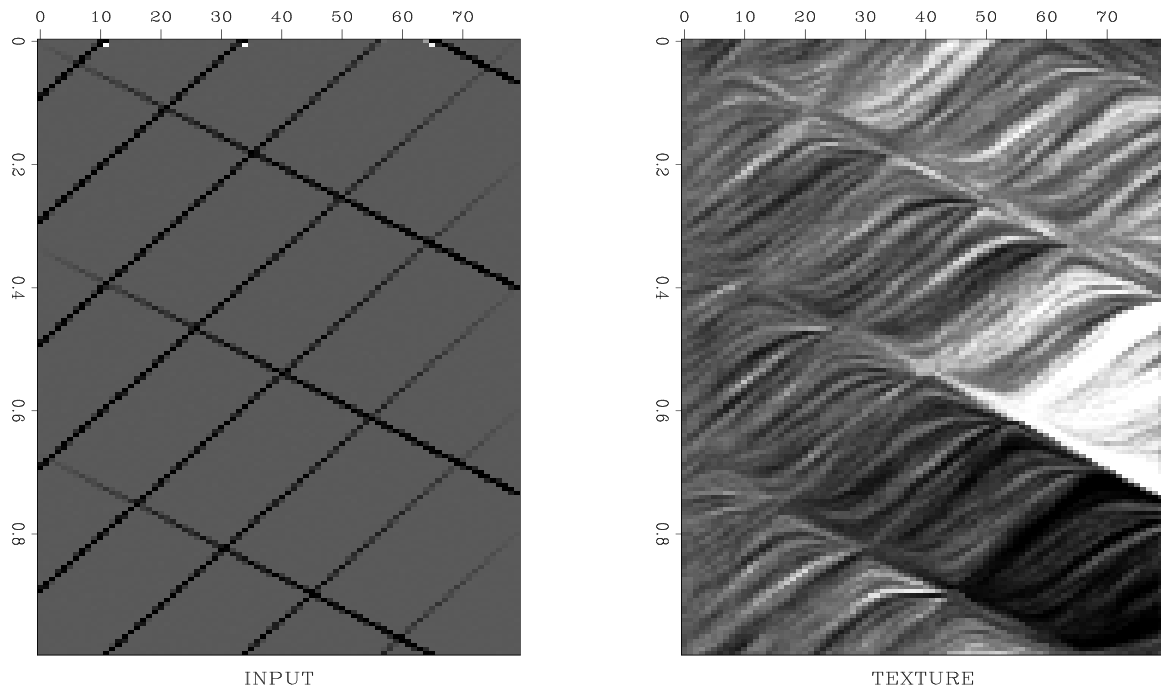
Figure 4: Conflicting dips synthetic. Left plot: Input data. Right plot: Its texture. sergey1-txtr-conflict [ER]

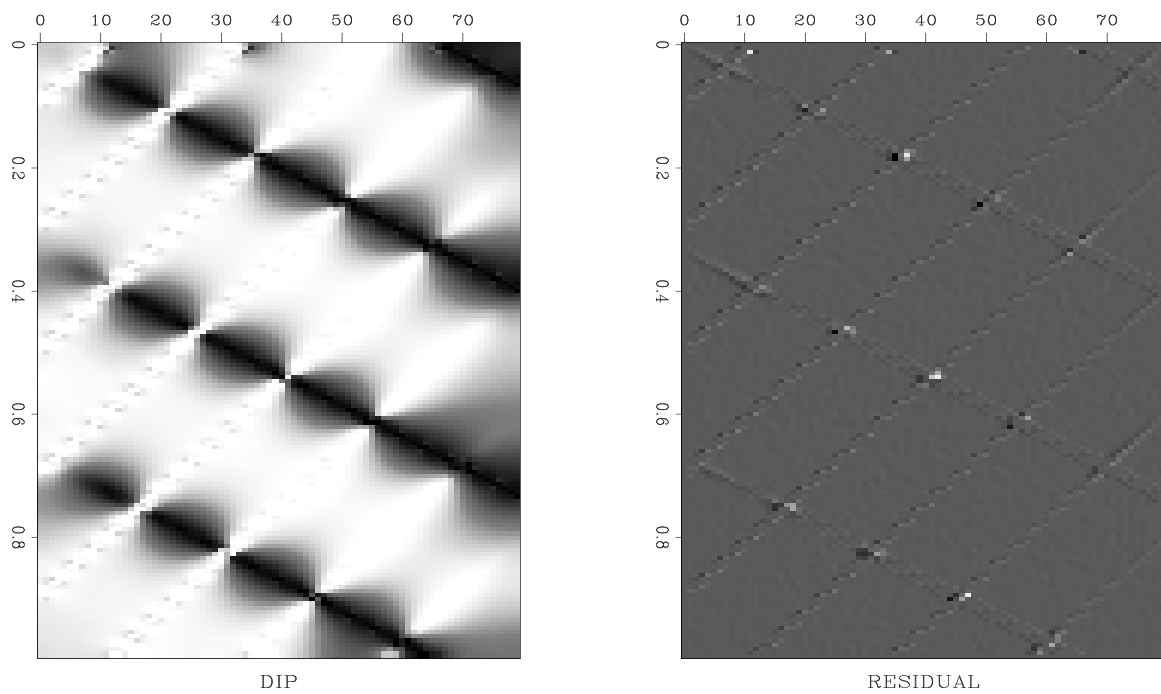Figure 5: Conflicting dips synthetic. Left plot: Estimated dip field. Right plot: Prediction residual. sergey1-lomo-conflict [ER]

set 27). The initial dip in the dip estimation program was set to zero. Therefore, the texture image (the right plot in Figure 6) contains zero-dipping plane waves in the places of no data. Everywhere else the dip is accurately estimated from the data. The data contain a missing trace at about 0.7 km offset and a slightly shifted (possibly mispositioned) trace at about 1.1 km offset. The mispositioned trace is clearly visible in the dip estimate (the left plot in Figure 7), and the missing trace is emphasized in the residual image (the right plot in Figure 7). Additionally, the residual image reveals the forward and back-scattered surface waves, hidden under more energetic reflections in the input data.
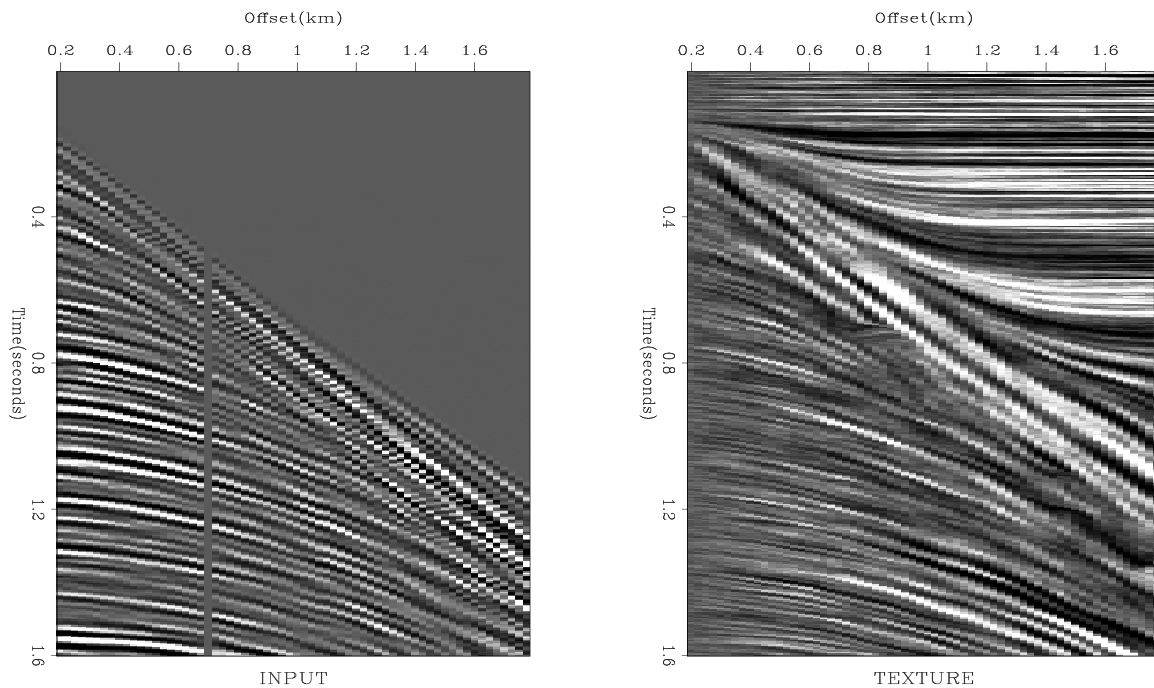

Figure 6: Real shot gather. Left plot: Input data. Right plot: Its texture. sergey1-txtr-yc27 [ER]

Figure 8 shows a stacked time section from the Gulf of Mexico and its corresponding texture. The texture plot demonstrates that the estimated dip (the left plot of Figure 9) reflects the dominant local dip in the data. After the plane waves with that dip are removed, many hidden diffractions appear in the residual image (the right plot in Figure 9.) The enhanced diffraction events can be used, for example, for estimating the medium velocity (Harlan et al., 1984).

Overall, the examples of this subsection show that the finite-difference plane-wave destructors are a reliable tool for enhancement of discontinuities and conflicting slopes in seismic images. The estimation step of the fault detection procedure produces an image of the local dip field, which may have its own interpretational value. An extension to 3-D is possible, as outlined by Claerbout (1993), Schwab (1998), Fomel (1999), and Clapp (2000a).
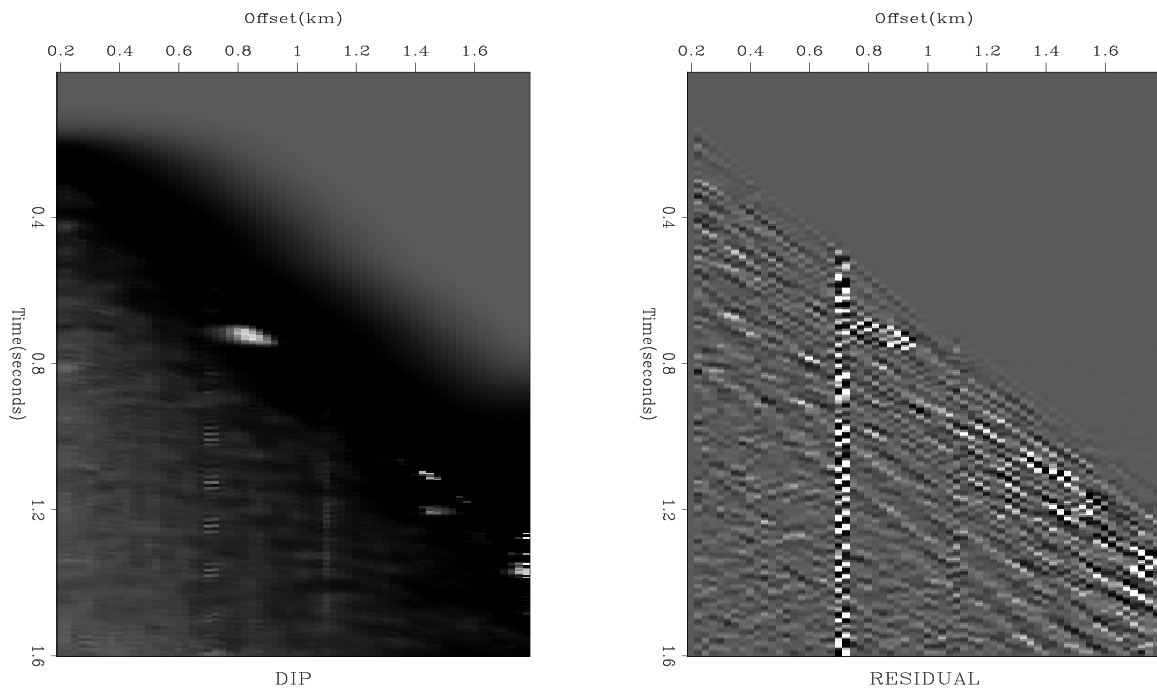
Figure 7: Real shot gather. Left plot: Estimated dip field. Right plot: Prediction residual.
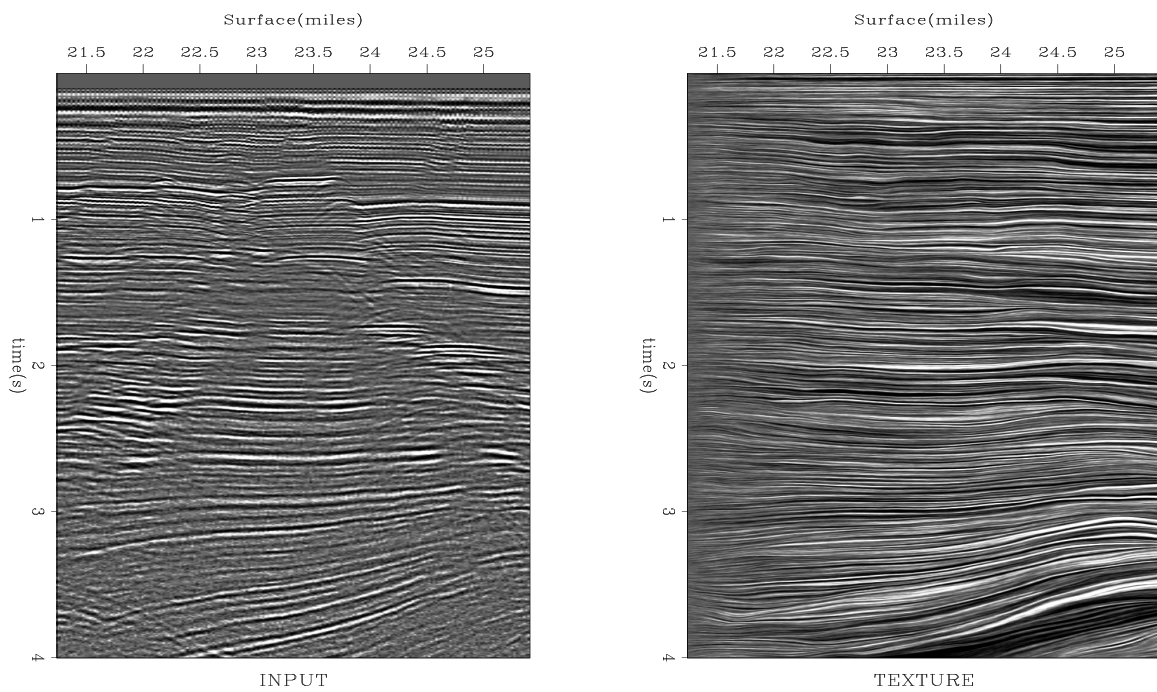sergey1-lomo2-yc27 [ER]

Figure 8: Time section from the Gulf of Mexico. Left plot: Input data. Right plot: Its texture.
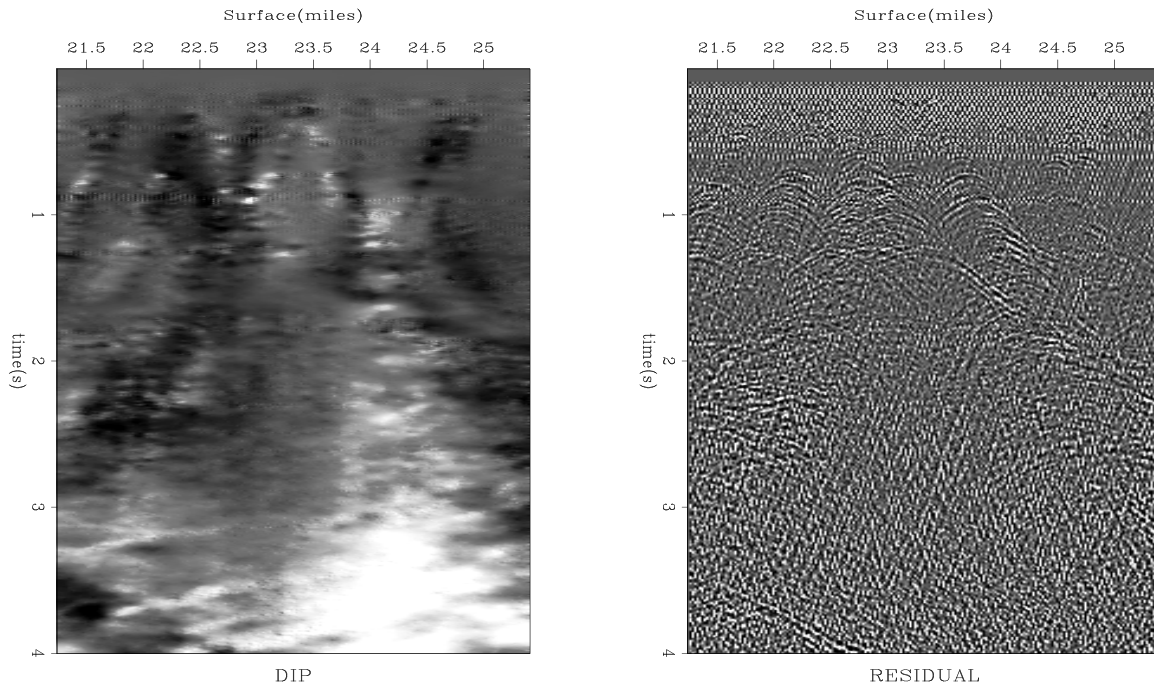sergey1-txtr-dgulf [ER]

Figure 9: Time section from the Gulf of Mexico. Left plot: Estimated dip field. Right plot: Prediction residual. sergey1-lomo-dgulf [ER]

Gap interpolation

Irregular gaps occur in the recorded data for many different reasons, and prediction-error filters are known as a powerful method for interpolating them. Interpolating irregularly spaced data also reduces to gap interpolation after binning.

Figure 10 shows a simple synthetic example of gap interpolation from Claerbout (1999). The input data has a large elliptic gap cut out from a two plane-wave model. I estimate both dip components from the input data by using the method of equations (16-18). The initial values for the two local dips were 1 and 0, and the estimated values are close to the true dips of 2 and -1 (two middle plots in Figure 10.) Although the estimation program did not make any assumption about dip being constant, it correctly estimated nearly constant values with the help of regularization equations (17-18). The rightmost plot in Figure 10 shows the result of gap interpolation with a two-plane local plane-wave destructor. The result is nearly perfect and compares favorably with the analogous result of the T-X PEF technique (Claerbout, 1999).

Figure 11 is another benchmark gap interpolation example from Claerbout (1999). The data are ocean depth measurements from one day SeaBeam acquisition. The data after normalized binning are shown in the left plot of Figure 11. From the known part of the data, we can partially see a certain elongated and faulted structure on the ocean floor. Estimating a smoothed dominant dip in the data and interpolating with the plane-wave destructor filters produces the image in the right plot of Figure 11. The V-shaped acquisition pattern is somewhat visible in the interpolation result, which might indicate the presence of a fault. Otherwise,

original   gapped   first dip   second dip   restored
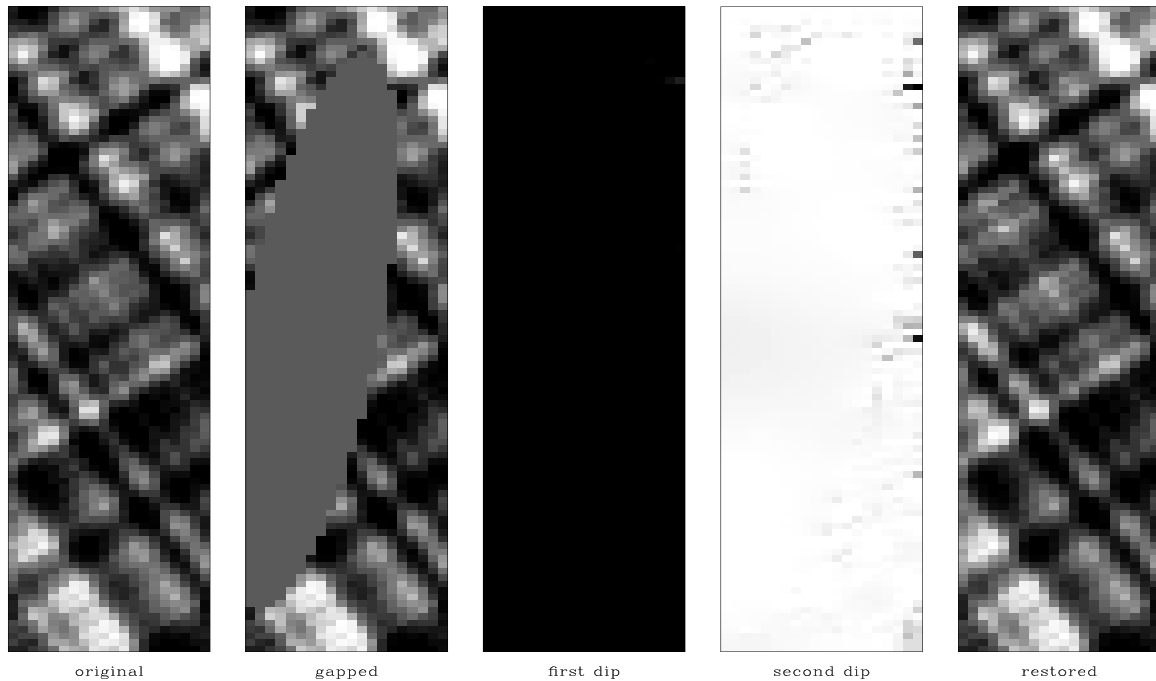
Figure 10: Synthetic gap interpolation example. From left to right: original data, input data, first estimated dip, second estimated dip, interpolation output. sergey1-hole [ER]

the result is both visually pleasing and fully agreeable with the data. Clapp (2000b) shows on the same data example how to obtain multiple statistically equivalent realizations of the interpolated data.

A 3-D interpolation example is shown in Figure 12. The input data resulted from a passive seismic experiment (Cole, 1995) and originally contained many gaps because of instrument failure. I interpolated the 3-D gaps with a pair of two orthogonal plane-wave destructors in the manner proposed by Schwab and Claerbout (1995) for T-X prediction filters. The interpolation result shows a visually pleasing continuation of locally plane events through the gaps. It compares favorably with an analogous result of a stationary T-X PEF.

We can conclude that plane-wave destructors provide an effective method of gap filling and missing data interpolation.

Trace interpolation beyond aliasing

Spitz (1991) popularized the application of prediction-error filters to regular trace interpolation and showed how the spatial aliasing restriction can be overcome by scaling the frequencies of F-X PEFs. An analogous technique for T-X filters was developed by Claerbout (1992a, 1999) and applied for 3-D interpolation with non-stationary PEFs by Crawley (2000). The T-X technique implies stretching the filter in all directions so that its dip spectrum is preserved, while the coefficients can be estimated at alternating traces. After the filter is estimated, it
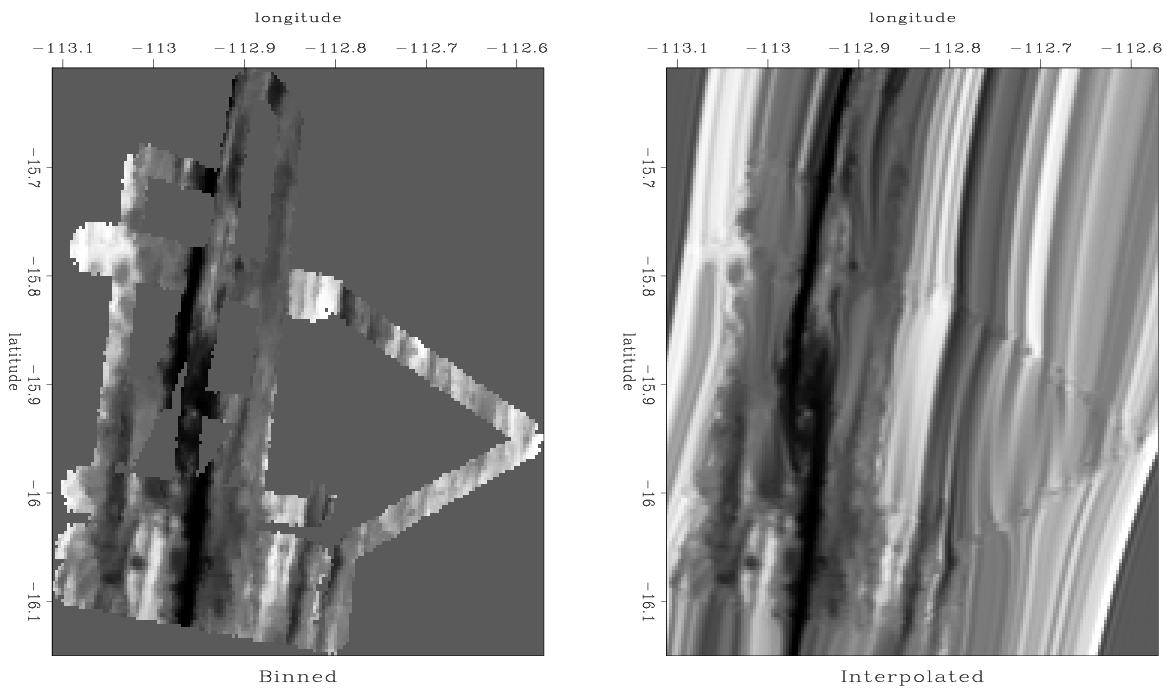
Figure 11: Depth of the ocean from SeaBeam measurements. Left plot: after binning. Right plot: after binning and gap interpolation. sergey1-seab [ER,M]
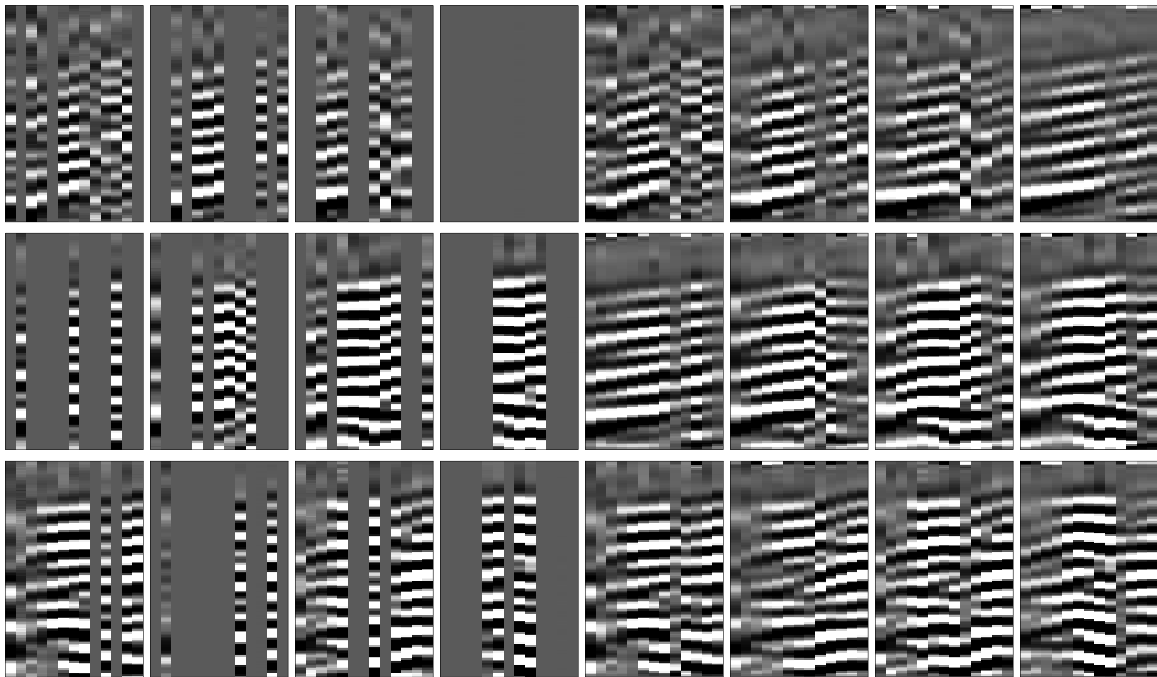

Figure 12: 3-D gap interpolation in passive seismic data. The left 12 panels are slices of the input data. The right 12 panels are the corresponding slices in the interpolation output. sergey1-passfill [ER,M]

is scaled back and used for interpolating missing traces in between the known ones. A very similar method works for finite-difference plane wave destructors, only we need to take a special care to avoid aliased dips at the dip estimation stage.

Figure 13 shows a marine 2-D shot gather from a deep water Gulf of Mexico survey before and after subsampling in the offset direction. The data are similar to those used by Crawley (2000). The shot gather has long-period multiples and complicated diffraction events caused by a salt body. Subsampling by a factor of two (the right plot in Figure 13) causes a clearly visible aliasing in the steeply dipping events. The goal of my first experiment was to interpolate the missing traces in the subsampled data and to compare the result with the original gather shown in the left plot of Figure 13.
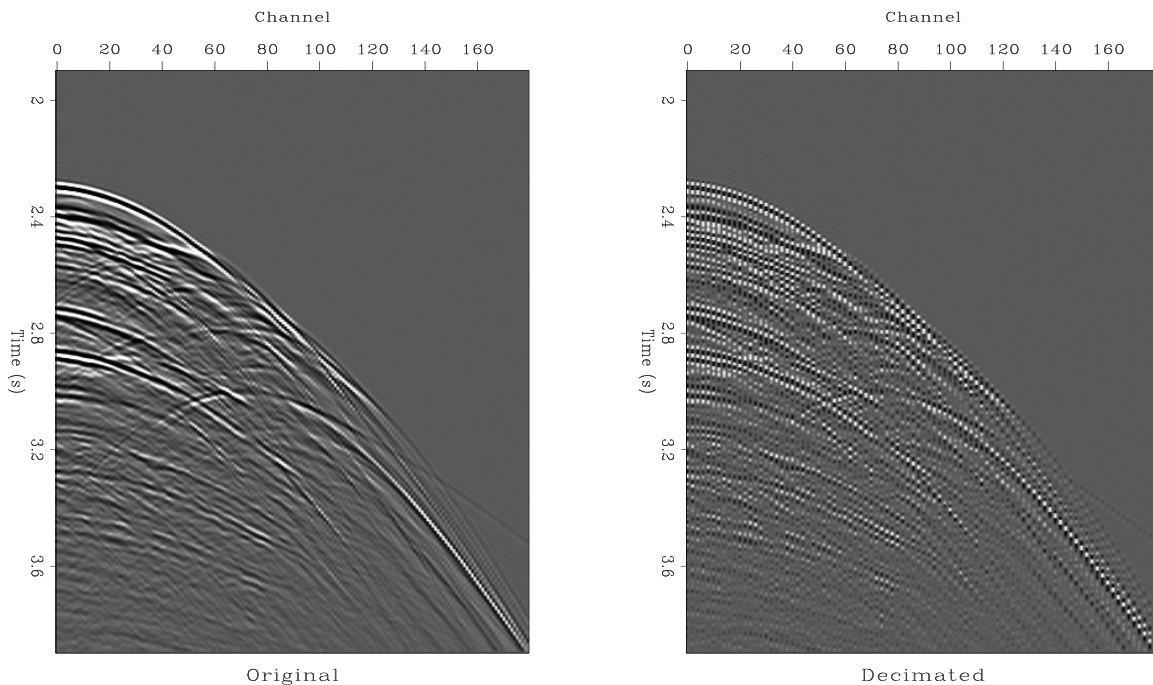

Figure 13: 2-D marine shot gather. Left: original. Right: subsampled by a factor of two in the offset direction. sergey1-sean2 [ER]

A straightforward application of the dip estimation equations (16-18) applied to aliased data can easily lead to erroneous aliased dip estimation. In order to avoid this problem, I chose a slightly more complex strategy. The algorithm for trace interpolation of aliased data consists of the following steps:

1. Applying Claerbout's T-X methodology, stretch a two-dip plane-wave destructor filter and estimate the dips from decimated data.

2. The second estimated dip will be infected by aliasing. Ignore this initial estimate.

3. Estimate the second dip component again by fixing the first dip component and using it as the initial estimate of the second component. This trick prevents the nonlinear estimation algorithm from picking the wrong (aliased) dip in the data.

4. Down-scale the estimated two-dip filter and use it for interpolating missing traces.

The two estimated dip components are shown in Figure 14. The first component contains only positive dips. The second component coincides with the first one in the areas where only a single dip is present in the data. In other areas, it picks the complimentary dip, which has a negative value for back-dipping hyperbolic diffractions.
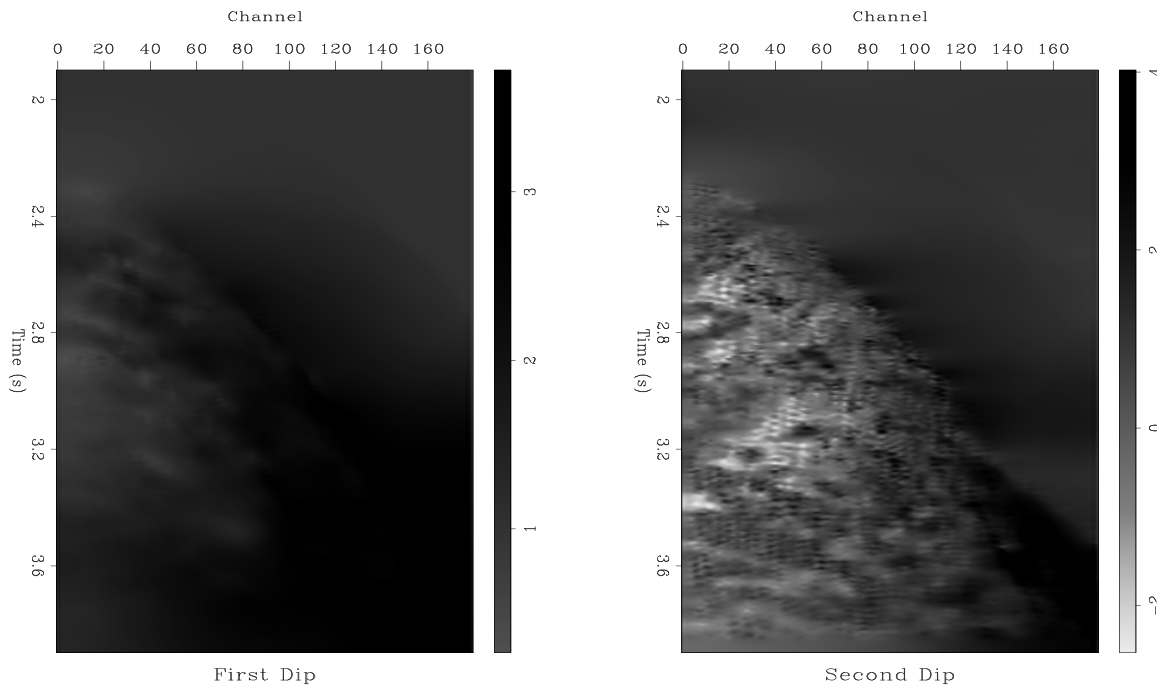

Figure 14: Two components of the estimated dip field for the decimated 2-D marine shot gather. sergey1-sean2-dip [ER]

Figure 15 shows the interpolation result and the difference between the interpolated traces and the original traces, plotted at the same clip value. The method succeeded in the sense that it is impossible to distinguish interpolated traces from the interpolation result alone. However, it is not perfect in the sense that some of the original energy is missing in the output. A closeup comparison between the original and the interpolated traces in Figure 16 shows that imperfection in more detail. Some of the steepest events in the middle of the section are poorly interpolated, and in some of the other places, the second dip component is continued instead of the first one.

The interpolation result can be considerably improved by including another dimension. To achieve a better result, we can use a pair of plane-wave destructors, one predicting local plane waves in the offset direction, and the other predicting local plane waves in the shot direction.
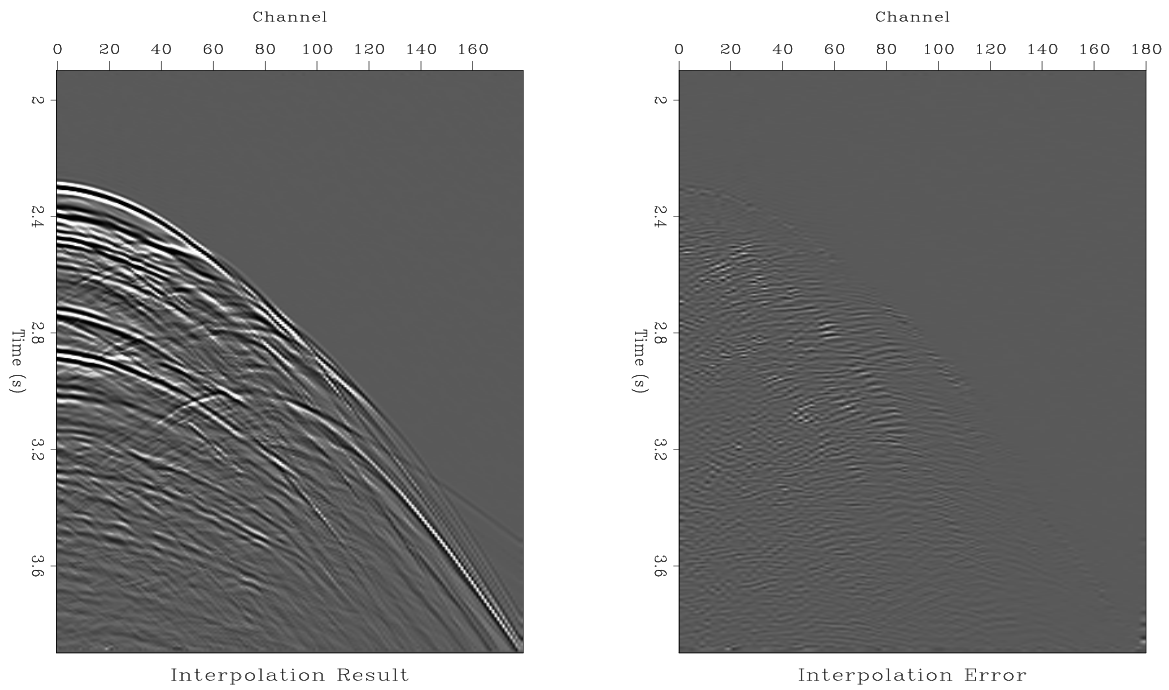
Figure 15: Left: 2-D marine shot gather after trace interpolation. Right: Difference between the interpolated and the original gather. sergey1-sean2-int [ER]
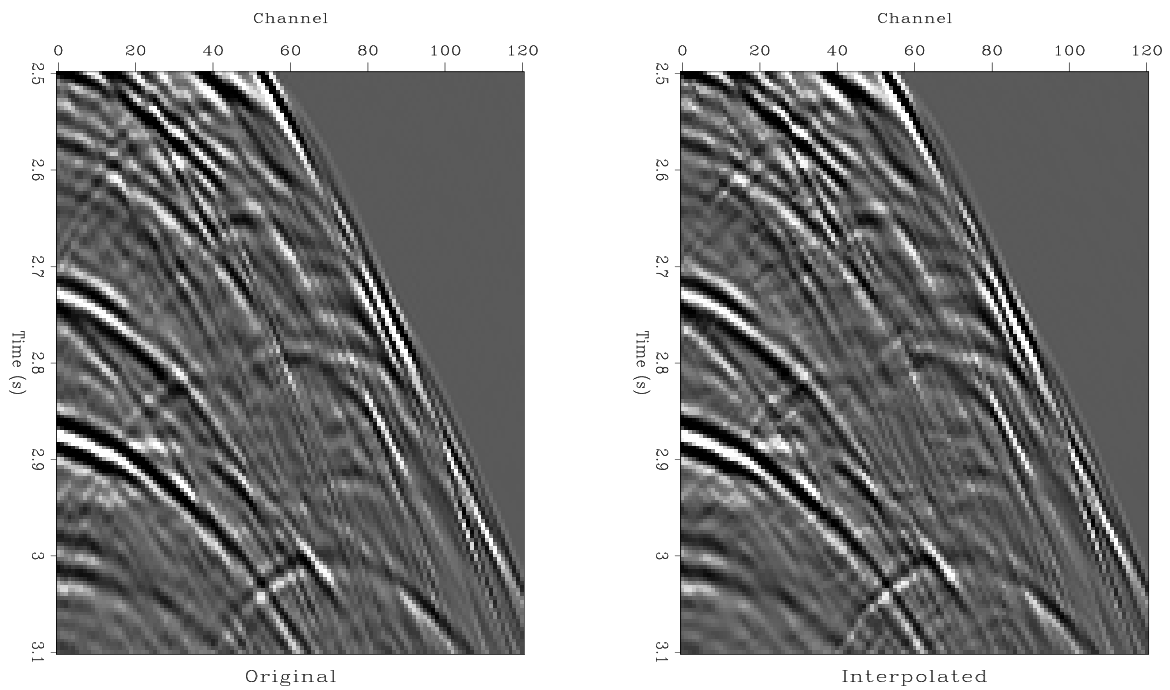

Figure 16: Close-up comparison of the interpolated (right) and the original data (left). sergey1-sean2-close [ER,M]

Signal and noise separation

Signal and noise separation and noise attenuation are yet another important application of plane-wave prediction filters (Canales, 1984; Abma, 1995; Soubaras, 1995; Spitz, 1999; Brown et al., 1999; Clapp and Brown, 2000; Claerbout and Fomel, 2000).

The problem has a very clear interpretation in terms of the local dip components. If two components, $\mathbf{s}_1$ and $\mathbf{s}_2$ are estimated from the data, and we can interpret the first component as signal, and the second component as noise, then the signal and noise separation problem reduces to solving the least-squares system

$$
\begin{aligned}
\mathbf{C}(\mathbf{s}_1)\mathbf{d}_1 &\approx 0\,, & (19) \\
\epsilon\mathbf{C}(\mathbf{s}_2)\mathbf{d}_2 &\approx 0 & (20)
\end{aligned}
$$

for the unknown signal and noise components $\mathbf{d}_1$ and $\mathbf{d}_2$ of the input data $\mathbf{d}$:

$$
\mathbf{d}_1 + \mathbf{d}_2 = \mathbf{d}. \tag{21}
$$

The scalar parameter ϵ in equation (20) reflects the signal to noise ratio. We can combine equations (19-20) and (21) in the explicit system for the noise component $\mathbf{d}_2$:

$$
\begin{aligned}
\mathbf{C}(\mathbf{s}_1)\mathbf{d}_2 &\approx \mathbf{C}(\mathbf{s}_1)\mathbf{d}\,, & (22) \\
\epsilon\mathbf{C}(\mathbf{s}_2)\mathbf{d}_2 &\approx 0\,. & (23)
\end{aligned}
$$

Figure 17 shows a simple example of the described approach. I estimated two dip components from the input synthetic data in a manner similar to that of Figure 10, and separated the corresponding events by solving the least-squares system (22-23). The separation result is visually perfect.

Figure 18 presents a significantly more complicated case: a receiver line from of a 3-D land shot gather from Saudi Arabia, contaminated with three-dimensional hyperbolic ground-roll. The same dataset has been used previously by Brown et al. (1999). The ground-roll noise and the reflection events have a significantly different frequency content, which might suggest an idea of separating them on the base of frequency alone. The result of frequency-based separation, shown in Figure 19 is, however, not ideal: part of the noise remains in the estimated signal after the separation. Changing the ϵ parameter in equation (23) could clean up the signal estimate, but it would also bring some of the signal into the subtracted noise. A better strategy is to separate the events by using both the difference in frequency and the difference in slope. For that purpose, I adopted the following algorithm:

1. Use a frequency-based separation (or, alternatively, a simple low-pass filtering) to obtain an initial estimate of the ground-roll noise.

2. Select a window around the initial noise. The further separation will happen only in that window.

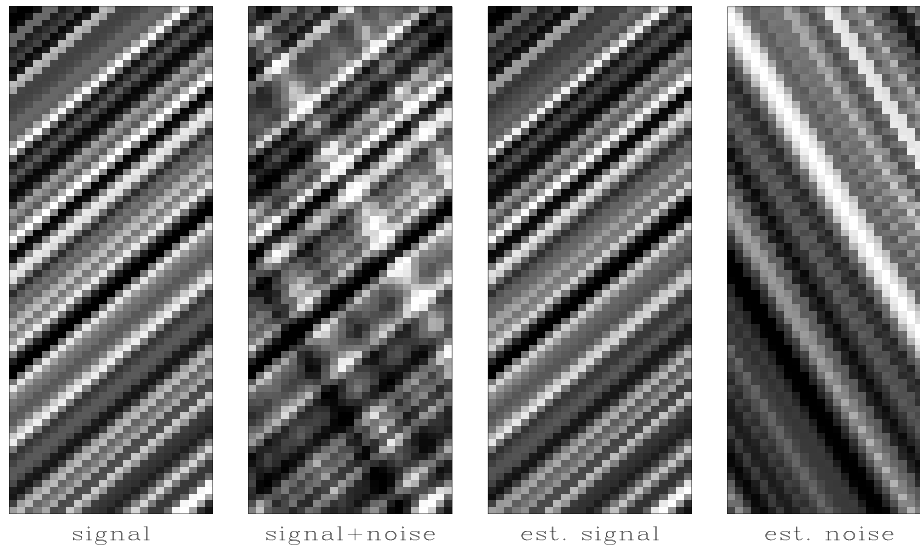3. Estimate the noise dip from the initial noise estimate.

signal   signal+noise   est. signal   est. noise

Figure 17: Simple example of dip-based single and noise separation. From left to right: ideal signal, input data, estimated signal, estimated noise. sergey1-sn2 [ER]

4. Estimate the signal dip in the selected data window as the complimentary dip component to the already known noise dip.

5. Use the signal and noise dips together with the signal and noise frequencies to perform the final separation. This is achieved by cascading single-dip plane-wave destructor filters with local 1-D three-coefficient PEFs, destructing a particular frequency.

The separation result is shown in Figure 20. The separation goal has been fully achieved: the estimated ground-roll noise is free of the signal components, and the estimated signal is free of the noise.

The left plot in Figure 21 shows another test example: a shot gather contaminated by nearly linear low-velocity noise. In this case, a simple dip-based separation was sufficient for achieving a good result. The algorithm proceeds as follows

1. Bandpass the original data with an appropriate low-pass filter to obtain an initial noise estimate (the right plot in Figure 21.)

2. Estimate the local noise dip from the initial noise model.

3. Estimate the signal dip from the input data as the complimentary dip component to the already known noise dip.

4. Estimate the noise by an iterative optimization of system (22-23) and subtract it from the data to get the signal estimate.
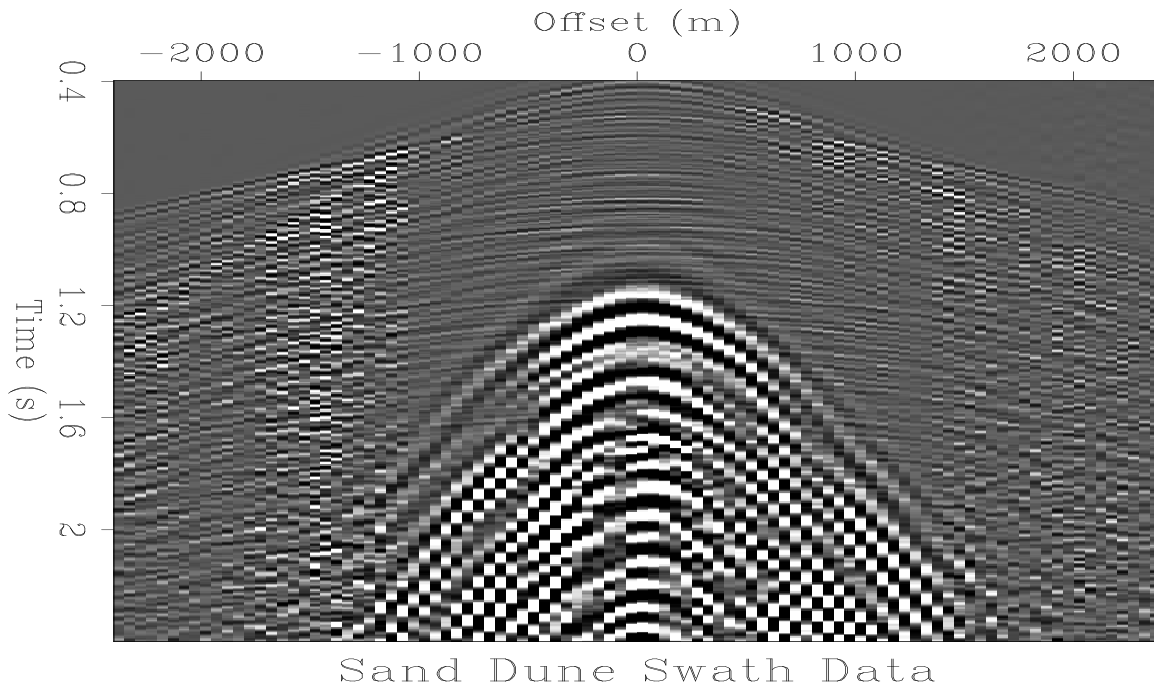
Figure 18: Ground-roll-contaminated data from Saudi Arabian sand dunes. A slice out of a 3-D shot gather. sergey1-dune-dat [ER]

Figure 22 shows the separation result. The signal and noise components are nicely separated. (Guitton, 2000) uses the same data example to develop a method of pairing noise separation with stacking velocity analysis.

The examples in this subsection show that when the signal and noise components have distinctly different local slopes, we can successfully separate them with plane-wave destructor filters.

CONCLUSIONS

The main conclusion of this paper is simple: plane-wave destructors with an improved finite-difference design can be a valuable tool in processing multidimensional seismic data. On several examples, I showed their good performance in such problems as fault detection, missing data interpolation, and noise attenuation. Further experiments will be necessary to gain more experience with plane-wave destructors and to improve the practical aspects of their usage.

It might be useful to summarize the similarities and differences between plane-wave destructors and T-X prediction-error filters.

Similarities:

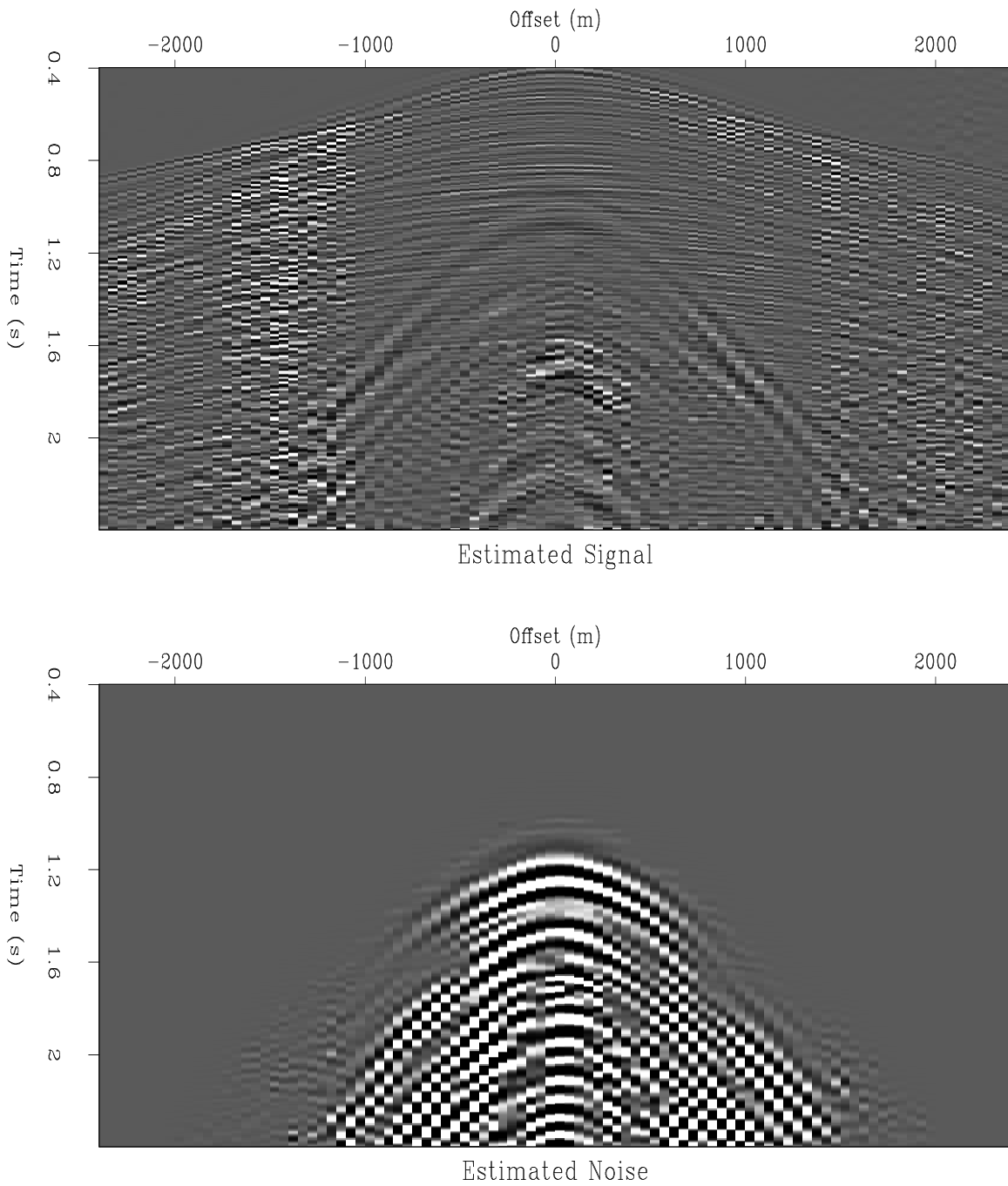- Both types of filters operate in the original time-and-space domain of recorded data.

Figure 19: Signal and noise separation based on frequency. Top: estimated signal. Bottom: estimated noise. sergey1-dune-exp [ER,M]
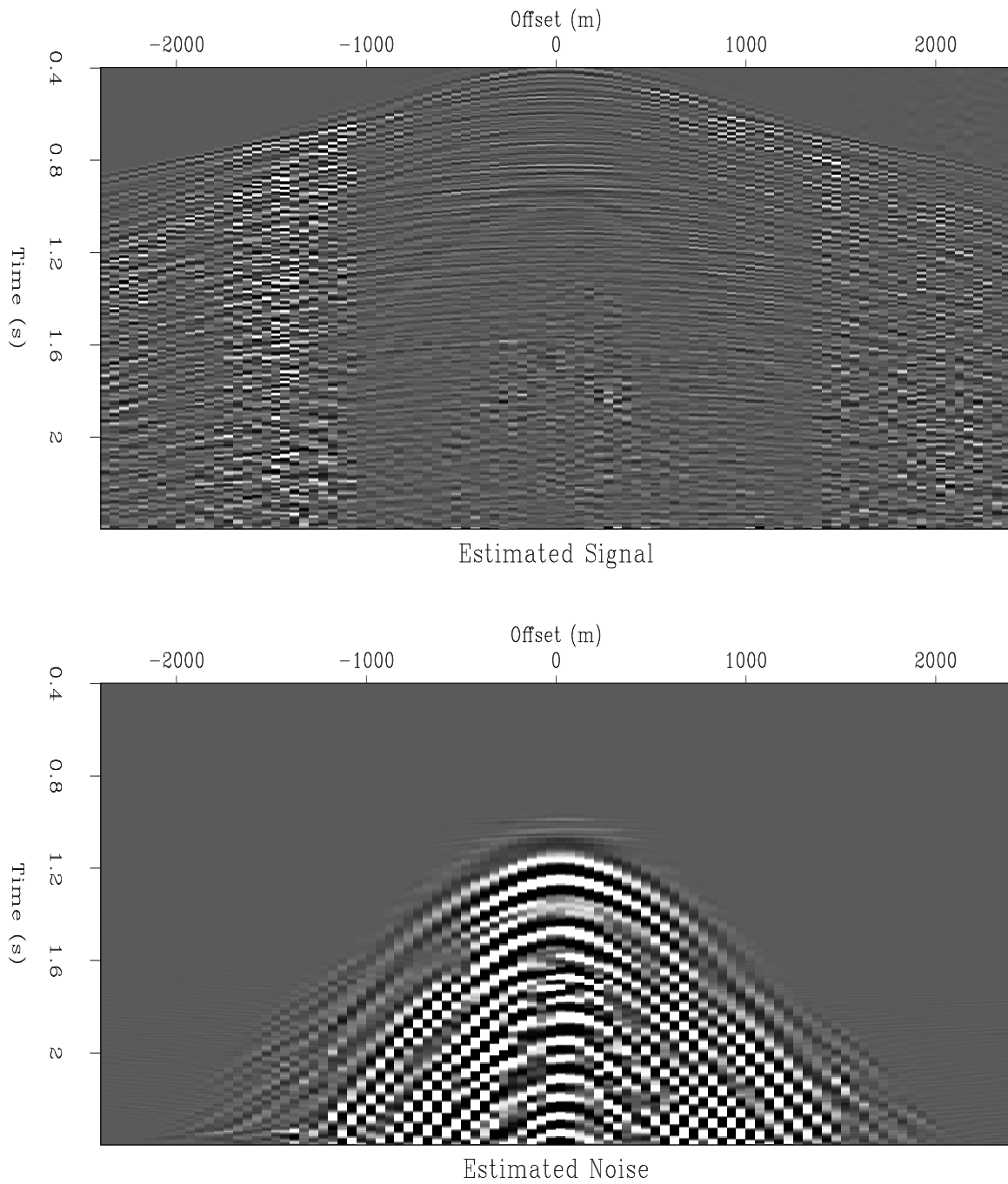
Figure 20: Signal and noise separation based on both dip and frequency. Top: estimated signal. Bottom: estimated noise. sergey1-dune-sn [ER,M]
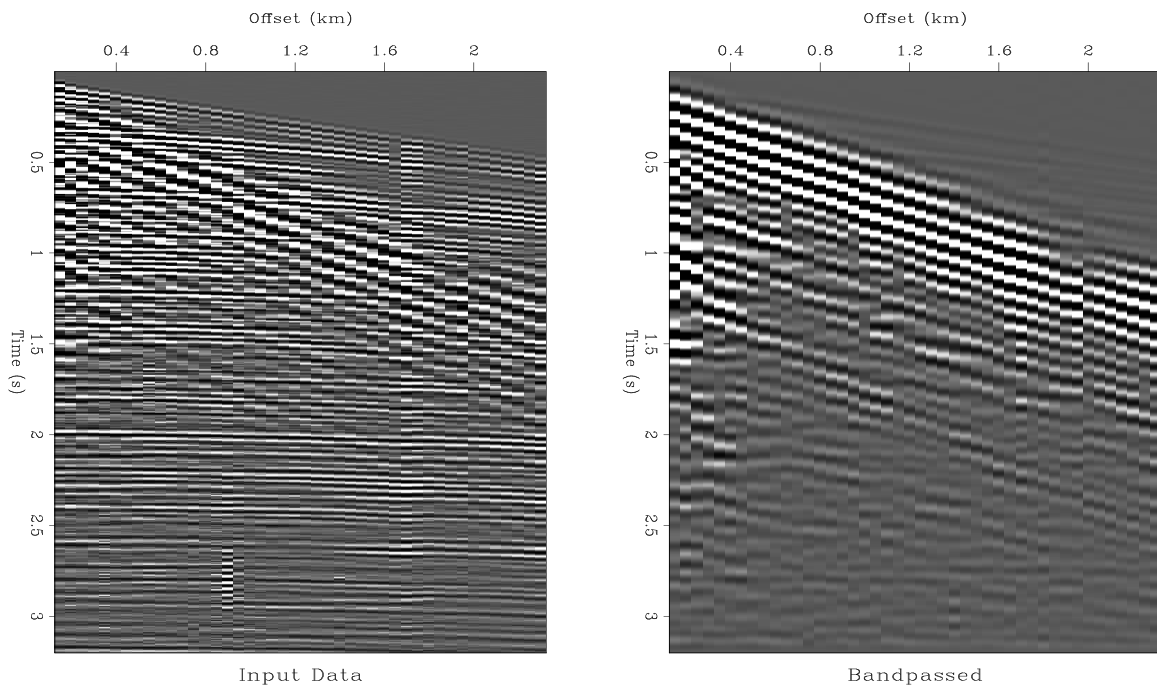
Figure 21: Left: Input noise-contaminated shot gather. Right: Result of low-pass filtering. sergey1-ant-dat [ER]
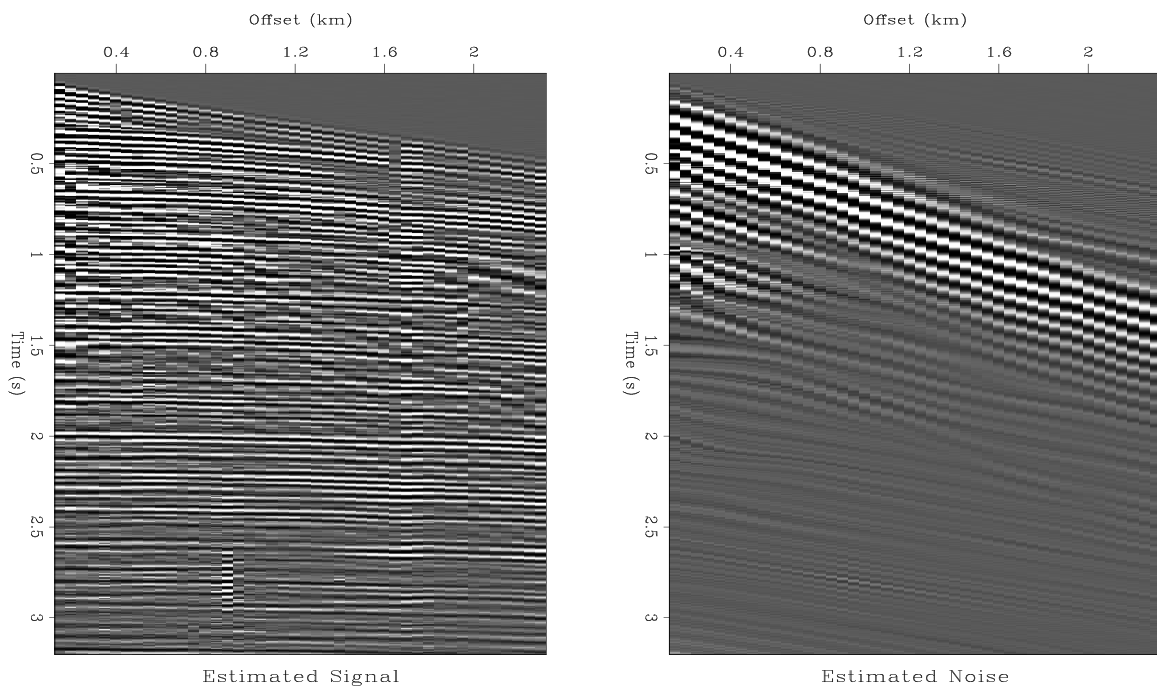
Figure 22: Signal and noise separation based on dip. Left: estimated signal. Right: estimated noise. sergey1-ant-sn [ER,M]

- Both filters aim at predicting local plane-wave events in the data.

- In most problems, one filter type can be replaced by the other, and certain techniques, such as Claerbout's trace interpolation method, are common for both approaches.

Differences:

- The design of plane-wave destructors is purely deterministic and follows the plane-wave differential equation. The design of T-X PEF has statistical roots in the framework of the maximum-entropy spectral analysis (Burg, 1975). In principle, T-X PEF can characterize more complex signals than local plane waves.

- In the case of PEF, we estimate filter coefficients. In the case of plane-wave destructors, the estimated quantity is the local plane slope. Several important distinctions follow from that difference:

  - The filter estimation problem is linear. The slope estimation problem, in the case of the improved filter design, is non-linear, but can be iteratively linearized. In general, non-linearity is an undesirable feature because of local minima and the dependence on initial conditions. However, we can sometimes use it creatively. For example, it helped me avoid aliased dips in the trace interpolation example.

  - Non-stationarity is handled gracefully in the local slope estimation. It is a much more difficult issue for PEFs because of the largely underdetermined problem.

  - Local slope has a clearly interpretable physical meaning, which allows for an easy quality control of the results. The coefficients of T-X PEFs are much more difficult to interpret.

- Plane-wave destructors are stable filters by construction. Stability is not guaranteed in the traditional PEF estimation and often can be a serious practical problem.

- The efficiency of the two approaches is difficult to compare. Plane-wave destructors are generally more efficient to apply because of the optimally small number of filter coefficients. However, they may require more computation at the estimation stage because of the already mentioned non-linearity problem.

ACKNOWLEDGMENTS

REFERENCES

Abma, R., 1995, Least-squares separation of signal and noise with multidimensional filters: Ph.D. thesis, Stanford University.

Bednar, J. B., 1997, Least squares dip and coherency attributes: SEP–**95**, 219–225.

Brown, M., Clapp, R. G., and Marfurt, K., 1999, Predictive signal/noise separation of groundroll-contaminated data: SEP–**102**, 111–128.

Brown, M., 1999, Texture synthesis and prediction error filtering: SEP–**100**, 211–222.

Burg, J. P., 1975, Maximum entropy spectral analysis: Ph.D. thesis, Stanford University.

Canales, L. L., 1984, Random noise reduction: 54th Annual Internat. Mtg., Soc. Expl. Geophys., Expanded Abstracts, Session:S10.1.

Claerbout, J., and Brown, M., 1999, Two-dimensional textures and prediction-error filters: 61st Mtg. Eur. Assoc. Expl. Geophys., Eur. Assoc. Expl. Geophys., Abstracts, Session:1009.

Claerbout, J., and Fomel, S., 2000, Spitz makes a better assumption for the signal PEF: SEP–**103**, 211–219.

Claerbout, J. F., 1992a, Earth Soundings Analysis: Processing Versus Inversion: Blackwell Scientific Publications.

Claerbout, J. F., 1992b, Information from smiles: Mono-plane-annihilator weighted regression: SEP–**73**, 409–420.

Claerbout, J. F., 1993, 3-D local monoplane annihilator: SEP–**77**, 19–25.

Claerbout, J., 1998, Multidimensional recursive filters via a helix: Geophysics, **63**, 1532–1541.

Claerbout, J., 1999, Geophysical estimation by example: Environmental soundings image enhancement: Stanford Exploration Project, http://sepwww.stanford.edu/sep/prof/.

Clapp, R. G., and Biondi, B. L., 1998, Regularizing time tomography with steering filters: SEP–**97**, 137–146.

Clapp, R. G., and Biondi, B. L., 2000, Tau tomography with steering filters: 2-D field data example: SEP–**103**, 1–19.

Clapp, R. G., and Brown, M., 2000, $(t − x)$ domain, pattern-based multiple separation: SEP–**103**, 201–210.

Clapp, R. G., Fomel, S., and Claerbout, J., 1997, Solution steering with space-variant filters: SEP–**95**, 27–42.

Clapp, R., Biondi, B., Fomel, S., and Claerbout, J., 1998, Regularizing velocity estimation using geologic dip information: 68th Ann. Internat. Meeting, Soc. Expl. Geophys., Expanded Abstracts, 1851–1854.

Clapp, R. G., Fomel, S., Crawley, S., and Claerbout, J. F., 1999, Directional smoothing of non-stationary filters: SEP–**100**, 197–209.

Clapp, R., 2000a, 3-D steering filters: SEP–**105**, 109–116.

Clapp, R., 2000b, Multiple realizations using standard inversion techniques: SEP–**105**, 67–78.

Cole, S. P., 1995, Passive seismic and drill-bit experiments using 2-D arrays: Ph.D. thesis, Stanford University.

Crawley, S., Clapp, R., and Claerbout, J., 1998, Decon and interpolation with nonstationary filters: SEP–**97**, 183–192.

Crawley, S., Clapp, R., and Claerbout, J., 1999, Interpolation with smoothly nonstationary prediction-error filters: 69th Ann. Internat. Meeting, Soc. Expl. Geophys., Expanded Abstracts, 1154–1157.

Crawley, S., 1999, Interpolation with smoothly nonstationary prediction-error filters: SEP–**100**, 181–196.

Crawley, S., 2000, Seismic trace interpolation with nonstationary prediction-error filters: Ph.D. thesis, Stanford University.

Fomel, S., Clapp, R., and Claerbout, J., 1997, Missing data interpolation by recursive filter preconditioning: SEP–**95**, 15–25.

Fomel, S., 1999, Plane wave prediction in 3-D: SEP–**102**, 101–110.

Fomel, S., 2000a, Helical preconditioning and splines in tension: SEP–**103**, 289–301.

Fomel, S., 2000b, Inverse B-spline interpolation: SEP–**105**, 79–108.

Fomel, S., 2000c, Seismic data interpolation with the offset continuation equation: SEP–**103**, 237–254.

Guitton, A., 2000, Coherent noise attenuation using Inverse Problems and Prediction Error Filters: SEP–**105**, 27–48.

Harlan, W. S., Claerbout, J. F., and Rocca, F., 1984, Signal/noise separation and velocity estimation: Geophysics, **49**, no. 11, 1869–1880.

Rickett, J., and Guitton, A., 2000, Multi-dimensional Fourier transforms in the helical coordinate system: SEP–**105**, 167–176.

Schwab, M., and Claerbout, J., 1995, The interpolation of a $3 - D$ data set by a pair of $2 - D$ filters: SEP–**84**, 271–278.

Schwab, M., Claerbout, J., and Holden, C., 1996a, Revealing geological discontinuities by plane reflector suppression: 66th Annual Internat. Mtg., Soc. Expl. Geophys., Expanded Abstracts, 302–305.

Schwab, M., Holden, C., and Claerbout, J., 1996b, Revealing geological discontinuities by local plane wave suppression: SEP–**92**, 29–47.

Schwab, M., 1998, Enhancement of discontinuities in seismic 3-D images using a Java estimation library: Ph.D. thesis, Stanford University.

Soubaras, R., 1995, Prestack random and impulsive noise attenuation by F-X projection filtering: 65th Annual Internat. Mtg., Soc. Expl. Geophys., Expanded Abstracts, 711–714.

Spitz, S., 1991, Seismic trace interpolation in the f-x domain: Geophysics, **56**, no. 6, 785–794.

Spitz, S., 1999, Pattern recognition, spatial predictability, and subtraction of multiple events: The Leading Edge, **18**, no. 1, 55–58.